

Achieving Near-Umity Red Light Photoluminescence in Antimony Halide Crystals via Polyhedron Regulation

Jin-Feng Liao⁺, Zhipeng Zhang⁺, Lei Zhou, Zikang Tang, and Guichuan Xing*

Abstract: Exploration of efficient red emitting antimony hybrid halide with large Stokes shift and zero self-absorption is highly desirable due to its enormous potential for applications in solid light emitting, and active optical waveguides. However, it is still challenging and rarely reported. Herein, a series of (TMS)₂SbCl₅ (TMS = triphenylsulfonium cation) crystals have been prepared with diverse [SbCl₅]²⁻ configurations and distinctive emission color. Among them, cubic-phase (TMS)₂SbCl₅ shows bright red emission with a large Stokes shift of 312 nm. In contrast, monoclinic and orthorhombic (TMS)₂SbCl₅ crystals deliver efficient yellow and orange emission, respectively. Comprehensive structural investigations reveal that larger Stokes shift and longer-wavelength emission of cubic (TMS)₂SbCl₅ can be attributed to the larger lattice volume and longer Sb···Sb distance, which favor sufficient structural aberration freedom at excited states. Together with robust stability, (TMS)₂SbCl₅ crystal family has been applied as optical waveguide with ultralow loss coefficient of 3.67·10⁻⁴ dB μm⁻¹, and shows superior performance in white-light emission and anti-counterfeiting. In short, our study provides a novel and fundamental perspective to structure-property-application relationship of antimony hybrid halides, which will contribute to future rational design of high-performance emissive metal halides.

Introduction

Over the past few years, organic-inorganic metal halides (OIMHs) have attracted enormous attention for their superior optoelectronic properties and solution-phase processability, which laid the solid foundation for their wide applications in display, lighting, and etc.^[1] Moreover, excellent structure tunability of OIMHs enabled the construction of multiple low-dimensional counterparts at the molecular level, including two-dimensional (2D) layers, one-dimensional (1D) chains, and zero-dimensional (0D) clusters.^[2] In contrast to the three-dimensional (3D) OIMHs usually with narrow-band emission, low-dimensional OIMHs can exhibit significantly distinct luminescence properties of large Stokes shift and broadband emission, as a result of the efficiently radiative recombination from self-trapped excitons (STEs). STEs are generally regarded as photogenerated transient defects induced by the large lattice distortion in the excited states.^[3] The “soft” nature combining with the strong electron-phonon coupling of the low-dimensional OIMHs pave the way for the ultrafast structural distortion upon excitation, conducive to the formation of STEs. Among the great family of OIMHs, of particular interest is 0D metal halides with isolated metal halide units, which can reinforce the quantum confinement effect and boost the exciton radiative recombination.^[4]

To address the structural lability issue and toxicity of lead-based metal halides, a large number of 0D Cu⁺, Sb³⁺, and Mn²⁺-based hybrid halides have been widely reported.^[5] Particularly, square-pyramidal structured antimony chlorides have been paid much attention due to its near-unity photoluminescence quantum yield (PQY) and outstanding structural stability.^[6] While after our systematical literature review (as can be seen in Figure S1a and Table S1), it is found that most of them exhibit yellow or orange emission color peaking at 590-620 nm and a Stokes shift about 250 nm due to restricted structure distortion freedom.^[7] Thus, it is highly desirable to obtain efficient red emitting antimony hybrid halide due to the urgent requirement of red phosphors for applications in solid light emitting, and active optical waveguides. However, exploration of efficient red emitting antimony hybrid halide with large Stokes shift is still challenging.^[8]

Diverse coordination modes have been reported in antimony halides through altering the organic ligands and the synthetic method, such as sphenoidal [SbCl₄]⁻, square-pyramidal [SbCl₅]²⁻, octahedral [SbCl₆]³⁻ and dimeric anions (e.g., [Sb₂Cl₇]⁻ and [Sb₂Cl₁₀]⁴⁻).^[8a,9] However, most of the antimony hybrid halides were synthesized by trial and error,

[*] Dr. J.-F. Liao,⁺ Dr. Z. Zhang,⁺ Prof. Z. Tang, Prof. G. Xing
Joint Key Laboratory of the Ministry of Education, Institute of Applied Physics and Materials Engineering
University of Macau
Macau, 999078, P. R. China
E-mail: gcxing@um.edu.mo

Prof. L. Zhou
School of Chemistry and Chemical Engineering
Southwest University
Chongqing, 400715, P. R. China

[†] These authors contributed equally.

© 2024 The Authors. *Angewandte Chemie* published by Wiley-VCH GmbH. This is an open access article under the terms of the Creative Commons Attribution Non-Commercial License, which permits use, distribution and reproduction in any medium, provided the original work is properly cited and is not used for commercial purposes.

and the design principle for custom synthesis is still unclear.^[8a,10] This is because understanding of the relationship between intrinsic structure distortion, coordination environment and optical property behind these highly emissive antimony halides is still rare.^[6c,11] Therefore, deeper understanding of structure–property relationship is still worth exploration.

Herein, a series of $(\text{TMS})_2\text{SbCl}_5$ crystals were synthesized with diverse $[\text{SbCl}_5]^{2-}$ configurations via a facile solvent engineering procedure. Their structural, optical, and electronic properties were further systematically analyzed. It is found that cubic phase $(\text{TMS})_2\text{SbCl}_5$ crystals possess the most symmetrical structure and show highly efficient red emission, while the distorted two counterparts (i.e., orthorhombic and monoclinic phases) exhibit yellow and orange emission color. Despite of different emission color, as-prepared three $(\text{TMS})_2\text{SbCl}_5$ crystals exhibited praiseworthy PLQY and robust stability, thus showing great potential application in optical waveguide, solid-state light, and anti-counterfeiting.

Results and Discussion

As depicted in Scheme S1, $(\text{TMS})_2\text{SbCl}_5$ single crystals were prepared via a traditional temperature cooling method using different solvents (for details, see the Experimental Section). All precipitated crystals are colorless under ambient light; however, different colored emission was observed under

365 nm UV light irradiation (Figure 1a). Red emission was observed in DMF derived crystals, while yellow and orange in ACN and DCM derived crystals, respectively. To confirm the vision disparity, steady state PL spectra were collected and shown in Figure 1b–d. The maximum emission peak was located at 664, 628 and 647 nm for DMF, ACN, and DCM derived crystals, respectively, with PLQY up to 90%. Three crystals also showed distinct light absorption behaviors, with an estimated optical band gap of 2.97, 3.07, 2.94 eV, respectively (Figure S2).

To shed light on the above-mentioned optical property differences, the crystal structures were characterized by single-crystal X-Ray diffraction (SCXRD) measurements. Crystallographic details are listed in Table S3–S8. As depicted in Figure 2a,d,g, three crystals were featured with a 0D periodic structure with isolated antimony chloride polyhedrons encircled by bulky organic cations. However, detailed analysis indicated noteworthy difference in antimony chloride polyhedron configurations. As for the DMF derived crystal, $(\text{TMS})_2\text{SbCl}_5$ was crystallized into cubic phase with cell parameters of $a=b=c=16.62 \text{ \AA}$, $\alpha=\beta=\gamma=90.0^\circ$. Each Sb atom is coordinated with five chlorine atoms, while six position have 83.3% occupancy factor due to extremely high symmetry. Similar phenomena have been previously reported in $(\text{C}_{25}\text{H}_{22}\text{P})_2\text{SbCl}_5$ and $(\text{MePPh}_3)_2\text{SbCl}_5$.^[12,13] By contrast, highly distorted square-pyramidal $[\text{SbCl}_5]^{2-}$ units were observed in the ACN and DCM derived $(\text{TMS})_2\text{SbCl}_5$ crystals, with orthorhombic space group of Pnma and monoclinic space group of P21/c,

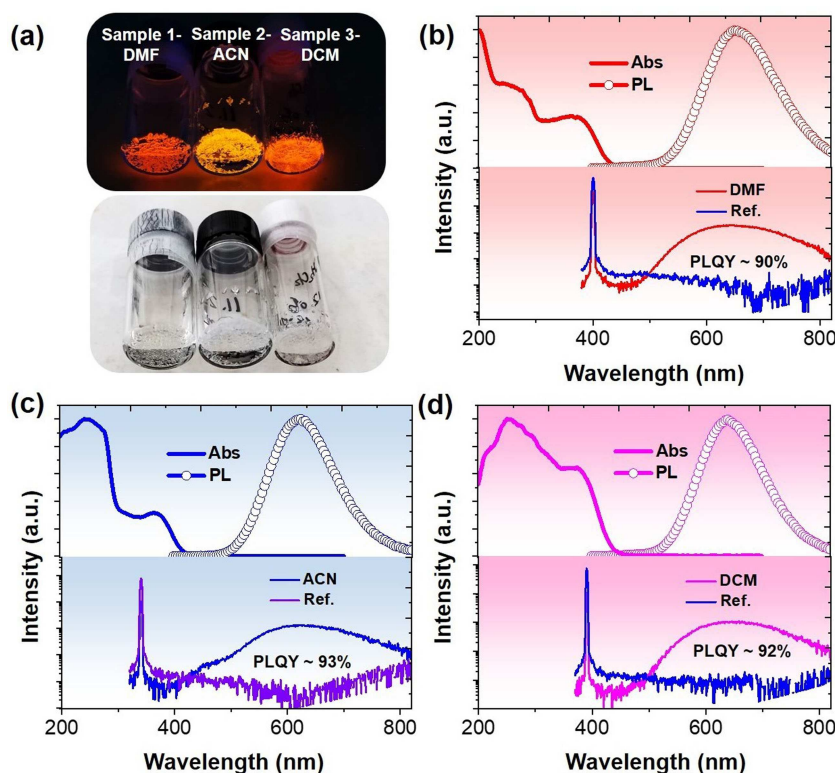


Figure 1. (a) Optical images of crystals under 365 nm UV light (up) and ambient light (down). UV/Vis light absorption, PL spectra and PLQY of (b) DMF, (c) ACN and (d) DCM derived samples.

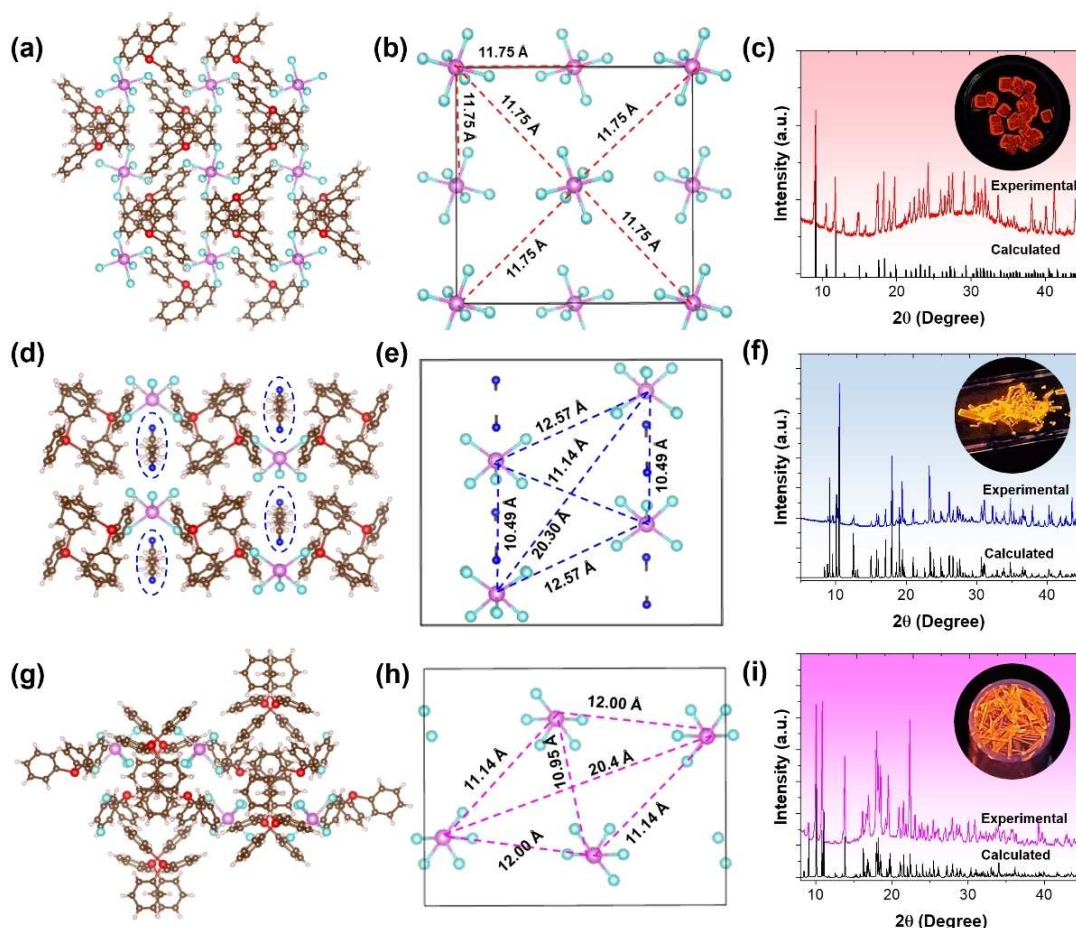


Figure 2. Crystal structures and unit cells of (a,b) DMF, (d,e) ACN and (g,h) DCM derived single crystals. Comparison of experimental and calculated PXRD patterns of (c) DMF, (f) ACN and (i) DCM derived samples. Inset are the optical images of crystals under excitation of 365 nm UV light.

respectively. In addition, it is interesting to find that ACN solvent molecular can co-crystallize with $(\text{TMS})_2\text{SbCl}_5$ affording a chemical formula of $(\text{TMS})_2\text{SbCl}_5 \cdot 2\text{ACN}$. The existence of ACN in crystal was further affirmed by infrared (IR) spectroscopy and hydrogen nuclear magnetic resonance (H NMR), as shown in Figure S3 and S4. As clearly shown in Figure 2d, the Cl–Sb–Cl bonds oriented to the nitrile ($\text{C}\equiv\text{N}$) groups of ACN exhibited larger bond angles compared to others, probably due to the electrostatic repulsion between Cl and N atoms. Detailed comparison of the bond angles in three crystals can be found in Tables S7–9. As a result of the same reason, $(\text{TMS})_2\text{SbCl}_5 \cdot 2\text{ACN}$ crystal possesses shortest Sb...Sb distance (10.49 Å) between adjacent $[\text{SbCl}_5]^{2-}$ clusters, compared to that of DMF (11.75 Å) and DCM (10.95 Å) derived crystals (Figure 2b,e and h). To quantify the geometry difference in these three crystals, the size of asymmetric coordination environment (σ^2) of the Sb^{3+} center was evaluated using the following equation:^[14]

$$\sigma^2 = \frac{1}{7} \sum_{i=1}^8 (a_i - 90^\circ)^2$$

where a_i represents the angle of Cl–Sb–Cl. The calculated σ^2 values are 0.02, 11.8 and 5.30 for DMF, ACN and DCM derived crystals, respectively. It suggests that the $[\text{SbCl}_5]^{2-}$ unit in ACN derived crystal is most distorted, while least distorted for DMF derived sample. Coincident conclusion can be further drawn from the comparison of Sb–Cl bond lengths (Figure S5). All Sb–Cl bonds in DMF derived crystal are in the same length of 2.553 Å. In the case of DCM derived crystals, the length of equatorial Sb–Cl bonds is similar about 2.600 Å, slightly longer than the axial position Sb–Cl bonds (2.380 Å). While as for $(\text{TMS})_2\text{SbCl}_5 \cdot 2\text{ACN}$ crystal, four equatorial Sb–Cl bonds are even highly different, ranging from 2.551 Å to 2.730 Å. The Sb–Cl bonds closer to the nitrile ($\text{C}\equiv\text{N}$) groups are much shorter due to electrostatic repulsion. The experimental powder XRD patterns agree well with the simulated patterns, confirming the reliability of the SCXRD refinement results (Figure 2c,f, and i). The inset are the optical images of crystals under excitation at 365 nm. Figure S6 represents the morphological

simulation data of three crystals, which agree well with experimental morphology. DMF derived crystals are almost equal in all directions, which facilitate an isotropic growth, while ACN and DCM derived crystals are rodlike, in accord with their different crystal systems. The phase purity could be verified by the homogeneous distribution of elements in these three crystals without phase separation (Figure S7). Furthermore, other organic solvents, such as methanol, chlorobenzene, toluene, acetone, ethyl acetate were also trialed (Figure S8a). As presented in Figure S8b, the resulted $(\text{TMS})_2\text{SbCl}_5$ exhibited a maximum emission peak at 648 nm, similar to the DCM derived crystals. Therefore, it can be inferred that monoclinic phase is thermodynamically preferred product, but slightly distinct crystallization kinetics appear in the ACN and DMF solvents system, thus leading to cubic and orthorhombic phase. The emissive properties of three crystals were further characterized via comprehensive wavelength-dependent PL and photoluminescence excitation (PLE) tests. As presented in Figure 3a-c, three crystals displayed tunable dual emission under high energy (HE)

light excitation, with additional low energy (LE) band peaking at 496, 475, 485 nm for the DMF, ACN and DCM derived crystal, respectively. The bimodal emission confers three crystals tunable PL colors under different energy light excitation (Figure S9a,d,g).

To confirm the nature of dual emissions, the corresponding PLE spectra are collected and depicted in Figure S9b,e,h. Three crystals showcased a broad PLE profile for LE emission band, while a sharp PLE band probed at HE emission band. The distinct difference of the PLE profile suggests that the dual-emission bands originate from different excited states. This conclusion can be further supported via the time-resolved PL tests. As shown in Figure S9c,f,i, the PL decay curves of two emission bands were fitted by a monoexponentially function, suggesting that the observed two emission bands possessed a single-exciton radiation, respectively. The lifetime of the LE emission band is 4.6, 3.8 and 4.4 μs for DMF, ACN and DCM derived crystal, respectively, while the HE emission lifetimes of three crystals are in the range of nanoseconds. Similar dual-

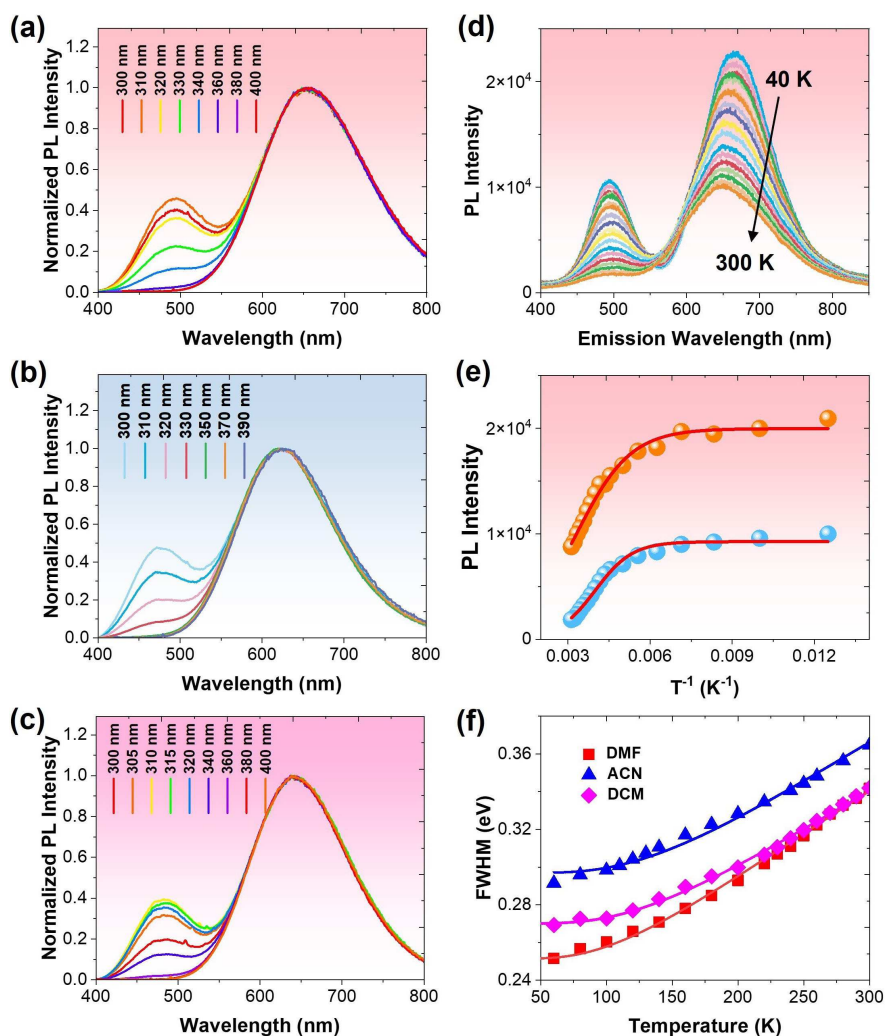


Figure 3. Excitation wavelength-dependent PL spectra of (a) DMF, (b) ACN and (c) DCM derived samples. (d) Temperature-dependent PL emission spectra of DMF derived crystal under excitation at 320 nm. (e) Plot of low energy (orange) and high energy (blue) band PL intensity versus temperature. (f) Comparison of the plot of low energy band PL FWHM versus temperature.

band emission behaviors were previously observed in Sb^{3+} -based metal halides, and the HE and LE emissions have been attributed to the transitions from singlet and triplet STEs, respectively.^[7a,12]

To gain deeper insight into the STE dynamics in the excited energy levels, femto-second transient absorption (fs-TA) spectra characterization was further carried out. As shown in Figure S10a, broad photo-induced absorption (PIA) was observed nearly covering the whole visible region when exciting at 400 nm laser, indicating the formation of additional excited-states in the below-gap region.^[15] When pumping with high energy laser (320 nm), two PIA signals were witnessed, corresponding to singlet and triplet STEs (Figure S10b). To shed light on the emissive mechanism, excitation power dependent PL tests have been carried out and the power exponent (k) was calculated via power-law equation (Figure S11):

$$I_{PL} = nL^k \quad (1)$$

where I_{PL} is PL intensity; L represents excitation power, and n is emission efficiency, k is power exponent and represents the recombination mechanism. Firstly, as the PL intensities exhibited linear dependence with respect to the excitation powers, the possibility of emission from permanent defects was ruled out.^[3] Due to the limited permanent defect concentration and long radiative recombination lifetime, typical permanent defects will easily approach to saturation point as excitation power increases, resulting in the non-linear power dependent photoluminescence with $k < 1$. Then, as the parameter k is fitted to be 1.02 (Figure S11b), the emission of $(\text{TMS})_2\text{SbCl}_5$ is originated from exciton-type recombination with intrinsic feature of STE rather than typical defect related recombination.^[16] STEs are self-trapped excitons because of intense coupling between excited excitons and structure lattice, and they will not easily get saturated under moderate range of excitation power, different from the easily saturated typical defects.^[16] In the case of highly emissive $(\text{TMS})_2\text{SbCl}_5$ with a high PLQY, the typical permanent defects will be saturated under low excitation power and thus play a negligible impact to power dependence curve.

To further elucidate the distinctive luminescence activities of these three crystals, their PL emission spectra were obtained from 40 to 300 K (Figure 3d, S13 and S14). It is worth noting that the PLQY value is excitation wavelength dependent, and it reduces from near unity to 50% when excited at 320 nm, as can be seen in Figure S12. When excited at 320 nm, excitons will be generated in high energy states (singlet states), and in this case, trap states capture process will fiercely compete with self-trapping and inter-system crossing transiting processes, thus leading to a moderate luminescence efficiency. When excited at 400 nm, excitons will be generated in lower energy states, and easily be self-trapped to STE₃ states, and thus the PLQY value is much higher. As shown in Figure 3d, both two band emission intensities increase monotonously as temperature decreases due to the subdued nonradiative recombination rate. In addition, the LE emission peak red-shifted slightly

for three crystals at low temperature, because of the competitive effects of the thermally induced crystal lattice expansion and electron-phonon coupling interaction.^[17] The exciton binding energy (E_b) can be calculated according to Arrhenius formula:

$$I(T) = \frac{I_0}{1 + A \exp(-\frac{E_b}{k_B T})} \quad (2)$$

where I_0 is the PL intensity at 0 K, and k_B is the Boltzmann constant. As shown in Figure 3e, S13c and S14c, the calculated E_b for singlet and triplet STEs are 87 and 126 meV for DMF derived crystal, 30 and 35 meV for ACN derived crystals, 63 and 90 meV for DCM derived crystals. The E_b values are larger than the thermal energy at room temperature (26 meV), which enables the STEs to overcome the thermal quenching. Notably, the emission spectra were broadened gradually with the temperature increasing because of the enhanced electron-phonon interaction in the soft crystal lattice of 0D hybrid halides. Furthermore, the electron-phonon interaction strength could be roughly evaluated by the Huang-Rhys (S) factor, which could be calculated through fitting the temperature-dependent FWHM curve according to the following equation,

$$FWHM = 2.36\sqrt{S} \hbar\omega_{\text{phonon}} \sqrt{\coth \frac{\hbar\omega_{\text{phonon}}}{2k_B T}} \quad (3)$$

where T is the temperature, and $\hbar\omega_{\text{phonon}}$ is the phonon energy. S factor was extracted as 11.3, 9.5 and 8.9 for DMF, ACN and DCM derived crystals, respectively (Figure 3f, S13d and S14d). In general, $S \geq 5$ signifies that strong coupling exists between electron and phonon.^[18] Here, all three crystals are demonstrated with strong electron-phonon interaction, which is beneficial for the STE formation. In addition, DMF derived crystal is characterized with larger S values, indicating relatively stronger electron-phonon coupling than the two other crystals. This is probably due to DMF derived crystal is featured with largest lattice volume and longest Sb...Sb distance, which offers a large lattice relaxation and distortion freedom. For this reason, it possesses a largest Stokes shift and lowest emission energy. Distinctively, ACN and DCM derived crystals possess larger ground-state structural distortion and smaller motion freedom at excited states, thus their Stokes shifts and FWHM are smaller than DMF derived crystal. Based on the above discussion, the comparison between structures and emissive properties of these three crystals are listed in Table 1.

Table 1: Comparison between optical properties of the three $(\text{TMS})_2\text{SbCl}_5$ crystals.

Crystal system	E_g /eV	PL /nm	$\tau/\mu\text{s}$	FWHM/nm	Stokes shift/eV	σ^2	S
cubic	2.97	664	4.6	130	1.65	0.02	11.3
orthorhombic	3.07	628	3.8	116	1.59	11.8	9.5
monoclinic	2.94	647	4.4	116	1.22	5.3	8.9

Generally, it is expected that larger structural distortions may lead to larger Stokes shifts and broader emissions for LMHP. However, here, we offered a new insight into the relationship between the distortion degree of the intrinsic metal halide units and the broadband emission. To further highlight the uniqueness of cubic $(\text{TMS})_2\text{SbCl}_5$, we have compared its emission peak and Stokes shift with previously reported square pyramidal $[\text{SbCl}_5]^{2-}$ based antimony halides (Figure S1a and Table S1). Most of the previously reported A_2SbCl_5 crystals own a maximum emission peak at about 600–620 nm, while in a sharp contrast cubic phased $(\text{TMS})_2\text{SbCl}_5$ could emit red colored emission peaking at 664 nm. In addition, we also compared the emissive parameters of cubic $(\text{TMS})_2\text{SbCl}_5$ with other red lead-free metal halides. As shown in Figure S1b and Table S2 and S12, it can be inferred that our material demonstrates a commendably high PLQY, demonstrating great potential in solid state light emitting applications.

Based on the above results and discussion, the simplified emission mechanism of these three crystals is described in Figure 4a. Upon excitation, electrons will jump from ground state (GS) to singlet ($1P^1$) and triplet ($3P^1$) excited states, and then they undergo ultrafast self-trapping to singlet and triplet STE states, because of photo-induced deforming $[\text{SbCl}_5]^{2-}$ pyramid.^[9a,19] Finally, a HE and LE emission band can be witnessed simultaneously due to the radiative recombination of STEs. Precise control of the excitation wavelength could result in a dynamic population distribution in these two independent STE states, thus leading to tunable luminescence. This is the reason why only a single broad LE emission band can be observed under LE excitation. Three crystals shine different emission color under photoexcitation, which should be caused by their different crystal structures.

To gain atomic insights into the mechanism of the dual emission behavior in these antimony halides, we performed DFT calculations by taking ACN and DCM derived crystals

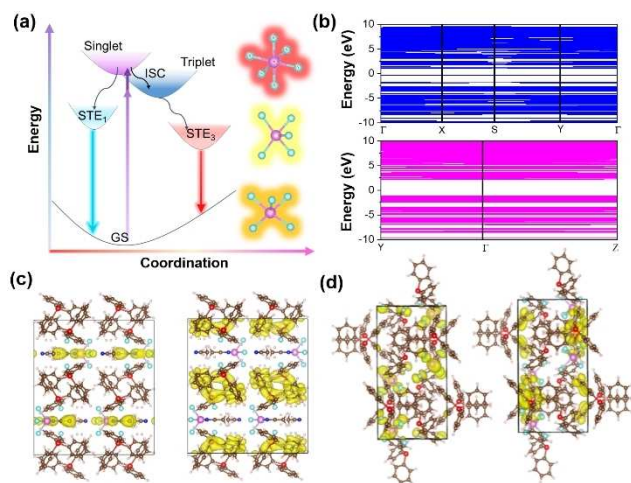


Figure 4. (a) Configuration diagrams of dual emission processes of three crystals. (b) DFT calculated band structures of ACN (top) and DCM (bottom) derived crystals. Calculated HOMO (left) and LUMO (right) for the ground states of (c) ACN and (d) DCM derived crystals.

as examples. As shown in Figure 4b, both two crystals possess relatively flat band dispersion, indicating weak coupling effect between $[\text{SbCl}_5]^{2-}$ clusters due to long Sb...Sb distance. Thus, light-generated excitons are completely confined to the isolated pentahedron, which is beneficial for efficient radiative recombination and high PLQY. In addition, the highest occupied molecular orbital (HOMO) of these two crystals is mainly composed of Sb-s and Cl-p characters, while lowest unoccupied molecular orbital (LUMO) consists mainly of organic counterpart (Figure 4c and d). Consistent result was found in the calculated density of states (DOS), which was presented in Figure S15. Clearly, the hybridization of Cl p and Sb s states dominantly contribute to the valence band maximum (VBM), while the conduction band minimum (CBM) is mainly dominated by the TMS^+ cations. Additionally, ACN molecule has an ignorable contribution to the LUMO and HOMO. Therefore, the underlying reason behinds the emission difference between ACN and DCM derived crystals is that after the ACN molecule entering the $(\text{TMS})_2\text{SbCl}_5$ crystal lattice, the bond length and bond angle of the individual $[\text{SbCl}_5]^{2-}$ will accordingly change, which in turn leads to different degrees of excited-state structural reorganization and thus different optical properties.

Inspired by the zero self-absorption and high PLQY as well as the long strip shape, DCM derived $(\text{TMS})_2\text{SbCl}_5$ crystal was further applied as optical waveguide. The schematic of the experimental setup is depicted in Figure 5a. As shown in Figure 5b, distance-dependent spatially re-

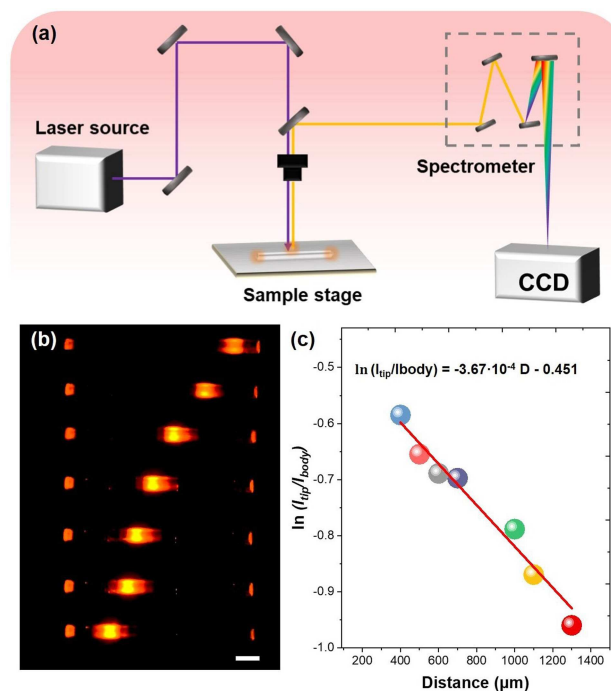


Figure 5. (a) Schematic illustration of the experimental setup for acquiring optical loss coefficient R . (b) The PL microscopy image of microrods obtained by excitation at different positions. (c) Fitted plot of $\ln(I_{\text{tip}}/I_{\text{body}})$ versus the distance between the excited site and the emitting tip. Scale bar: 200 μm .

solved PL images of the $(\text{TMS})_2\text{SbCl}_5$ single-crystalline microrod were recorded. Figure S16a, b show the PL spectra collected at the left emitting tip (I_{tip}) of the microrod. As shown in Figure 5c, the intensity ratio between the tips and bodies ($I_{\text{tip}}/I_{\text{body}}$) against the propagation distance reveals a nearly single exponential decay. To evaluate the waveguide activity, the optical loss coefficient (R) was estimated by using the function $I_{\text{tip}}/I_{\text{body}} = A \exp(-RD)$, where A is a constant and D is the distance between the excited body and the emitting tip.^[20] As a result, the optical loss coefficient R was calculated to be $3.67 \cdot 10^{-4} \text{ dB } \mu\text{m}^{-1}$, which is superior than that of most previously reported antimony halide crystals.^[21] Such low loss coefficient indicates efficient transmission of light-generated photon along the microrod with minimal optical loss, which can be attributed to negligible self-absorption and light scattering as a result of the large Stokes shift and high crystallinity. To further highlight the superior performance, we have compared the optical loss coefficient of $(\text{TMS})_2\text{SbCl}_5$ with other type metal hybrid halide crystals (Table S13).^[22]

In addition to the outstanding emissive properties, $(\text{TMS})_2\text{SbCl}_5$ crystals also exhibited exemplary resistance to heat and UV light. As shown in Figure S17, the initial PL intensity could be well remained after continuous heating at

70°C for 240 mins or under continuous UV light illumination for 180 mins. Of note is that a reversible transformation processes between ACN and DCM derived crystals is observed after heating $(\text{TMS})_2\text{SbCl}_5 \cdot 2\text{ACN}$ crystals at 70°C for about 10 mins or exposure in air for hours (Figure S18 and S19). The XRD patterns and PLE results of the transformed crystal are in well accord with fresh DCM derived crystals, which indicates that stripping of acetonitrile molecular transformed the $(\text{TMS})_2\text{SbCl}_5 \cdot 2\text{ACN}$ into $(\text{TMS})_2\text{SbCl}_5$ (Figure S18b,c). The phase-transformed crystal also exhibited a superior PLQY (Figure S18d).

To demonstrate the above properties (high PLQY, robust stability and tunable PL color), we fabricated a WLED device by mixing DCM derived $(\text{TMS})_2\text{SbCl}_5$ with two commercial phosphors (blue emissive $\text{BaMgAl}_{10}\text{O}_{17}:\text{Eu}$ and green emissive $(\text{SrBa})_2\text{SiO}_4:\text{Eu}$). As presented in Figure 6a, the WLED showed efficient warm white light with the derived color coordinates at (0.34, 0.34) under exciting with a 365 nm chip. $(\text{TMS})_2\text{SbCl}_5$ and these two commercial phosphors can nearly completely cover of the CIE diagram of the National Television System Committee (NTSC) standard color (Figure 6b). Furthermore, Figure 6c shows the films prepared by the $(\text{TMS})_2\text{SbCl}_5$ (left) and phosphor mixture (right) under 365 nm UV light. Figure 6d

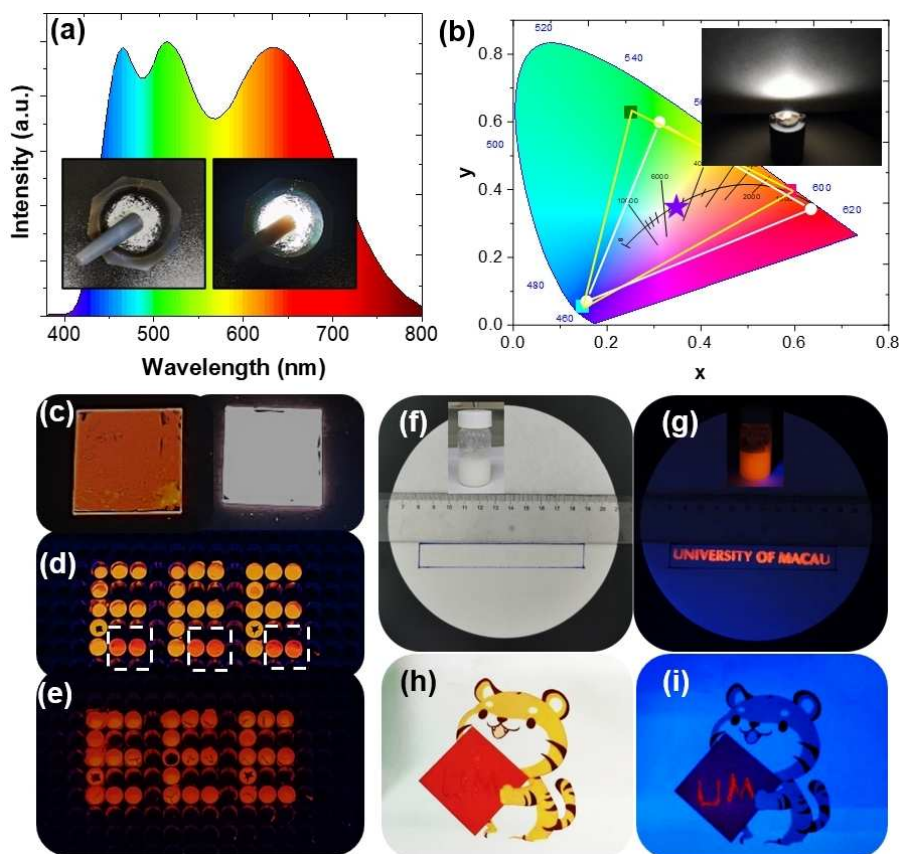


Figure 6. (a) The EL spectra of the WLED. Inset is the mixture under ambient light and 365 nm UV light. (b) The CIE chromaticity coordinate of the EL spectra (star) of WLED, and the CIE coordinates of the three phosphors (squares) compared to the NTSC color standards (circles). Inset is the photograph of WLED under operation. (c) The films prepared by the $(\text{TMS})_2\text{SbCl}_5$ (left) and mixture phosphor (right) under 365 nm UV light. (d-i) Application of $(\text{TMS})_2\text{SbCl}_5$ luminescent ink for anti-counterfeiting.

displays a misleading pattern encrypted with DCM and ACN derived crystals. Upon excitation at 365 nm, an orange “F” and a yellow “ ” appears, while it evolves into orange “E” after heating at 70 °C for 10 mins (Figure 6e). This is because the pattern “ ” that filled with ACN derived crystal will transform into (TMS)₂SbCl₅ due to the release of ACN molecular. Furthermore, (TMS)₂SbCl₅ powder could be further prepared as a luminescent ink, based on which, information can be readily encrypted on wiper. As shown in Figure 6f and h, the printed code “UNIVERSITY OF MACAU” and handwritten cope “UM” are invisible under ambient light due to the wide optical band gap of (TMS)₂SbCl₅, while these codes are readily observable with strong orange emission color under 365 nm excitation (Figure 6g and i).

Conclusion

In summary, three novel (TMS)₂SbCl₅ crystals have been successfully prepared with distinct emission color, red, orange, and yellow, respectively. With the in-depth structure-emission properties analysis, it is found that higher coordination symmetry and longer Sb–Sb distance are favor for the larger Stokes shift and lower energy emission. Thus, among the (TMS)₂SbCl₅ crystal family, cubic phase emits a lowest energy emission with a largest Stokes shift. Furthermore, reversible transformation was witnessed between yellow and orange emissive (TMS)₂SbCl₅ crystals upon the release/uptake of the ACN molecular. Due to exemplary emissive properties and stability, our proof-of-concept experiments demonstrated that (TMS)₂SbCl₅ family showed good performance in ultralow-loss optical waveguide, stable white light-emitting diode device, and anti-counterfeiting. This work not only provides a useful handle to directly achieve highly illuminative lead-free metal halide crystals, but also sheds mechanistic insights into the structure-photoluminescence-application relationship towards future development of highly efficient optoelectronic materials.

Supporting Information

Experimental procedures, and compound characterization data as well as computational details that support the findings of this study are available in the online version of this paper in the accompanying Supporting Information.

Acknowledgements

J.L. and Z.Z. contributed equally to this work. The authors acknowledge the Science and Technology Development Fund, Macao SAR (File no. FDCT-0044/2020/A1, 0082/2021/A2, 0010/2022/AMJ, 006/2022/ALC, 0136/2022/A3), UM's research fund (File no. MYRG2020-00151-IAPME, MYRG2022-00241-IAPME, MYRG-CRG2022-00009-FHS), the research fund from Wuyi University (EF38/IAPME-XGC/2022/WYU), the Natural Science Foundation

of China (61935017, 62175268, 62288102) and Shenzhen-Hong Kong-Macao Science and Technology Innovation Project (Category C) (SGDX2020110309360100).

Conflict of Interest

The authors declare no conflict of interest.

Data Availability Statement

The data that support the findings of this study are available from the corresponding author upon reasonable request.

Keywords: red light photoluminescence · optical waveguide · antimony halide crystal · polyhedron regulation

- [1] a) H. Gu, J. Xia, C. Liang, Y. Chen, W. Huang, G. Xing, *Nat. Rev. Mater.* **2023**, *8*, 533–551; b) Y. Han, X. Cheng, B.-B. Cui, *Mater Adv* **2023**, *4*, 355–373; c) F. Jiang, Z. Wu, M. Lu, Y. Gao, X. Li, X. Bai, Y. Ji, Y. Zhang, *Adv. Mater.* **2023**, 2211088; d) S. Wang, S. Feng, R. Li, J. Jin, J. Wu, W. Zheng, Z. Xia, X. Chen, Q. Ling, Z. Lin, *Adv. Mater.* **2023**, 2211992; e) S. Feng, Y. Ma, S. Wang, S. Gao, Q. Huang, H. Zhen, D. Yan, Q. Ling, Z. Lin, *Angew. Chem. Int. Ed.* **2022**, *61*, e202116511; f) B. Zhou, D. Yan, *Adv. Funct. Mater.* **2023**, *33*, 2300735; g) B. Zhou, Z. Qi, D. Yan, *Angew. Chem. Int. Ed.* **2022**, *61*, e202208735; h) C. Xing, B. Zhou, D. Yan, W. Fang, *CCS Chem.* **2023**, *5*, 2866–2876; i) Y. Lin, S. Liu, D. Yan, *Research* **2023**, *6*, 0259; j) B. Zhou, D. Yan, *Chem. Sci.* **2022**, *13*, 7429–7436.
- [2] a) L. Zhou, J. F. Liao, D. B. Kuang, *Adv. Mater.* **2021**, *9*, 2100544; b) C. He, X. Liu, *Light-Sci. Appl.* **2023**, *12*, 15.
- [3] J. Luo, X. Wang, S. Li, J. Liu, Y. Guo, G. Niu, L. Yao, Y. Fu, L. Gao, Q. Dong, C. Zhao, M. Leng, F. Ma, W. Liang, L. Wang, S. Jin, J. Han, L. Zhang, J. Etheridge, J. Wang, Y. Yan, E. H. Sargent, J. Tang, *Nature* **2018**, *563*, 541–545.
- [4] a) C. Zhu, J. Jin, Z. Wang, Z. Xu, M. C. Folgueras, Y. Jiang, C. B. Uzundal, H. K. D. Le, F. Wang, X. Zheng, P. Yang, *Science* **2024**, *383*, 86–93; b) B. Chen, Y. Guo, Y. Wang, Z. Liu, Q. Wei, S. Wang, A. L. Rogach, G. Xing, P. Shi, F. Wang, *J. Am. Chem. Soc.* **2021**, *143*(42), 17599–17606.
- [5] a) D. Banerjee, B. Saparov, *Chem. Mater.* **2023**, *35*, 3364–3385; b) J. B. Luo, J. H. Wei, Z. Z. Zhang, Z. L. He, D. B. Kuang, *Angew. Chem. Int. Ed.* **2023**, *135*, e202216504; c) Y. Shi, D. Liang, Q. Mo, S. Lu, Z. Sun, H. Xiao, Q. Qian, Z. Zang, *Chem. Commun.* **2023**, *59*, 583–586.
- [6] a) M. Yin, B. Li, Z. Yi, Y. Zhang, Z. Xia, Y. Xu, *Chem. Commun.* **2023**; b) D.-Y. Liu, H.-Y. Li, R.-P. Han, H.-L. Liu, S.-Q. Zang, *Angew. Chem. Int. Ed.* **2023**, e202307875; c) C. Sun, Z. Deng, Z. Li, Z. Chen, X. Zhang, J. Chen, H. Lu, P. Canepa, R. Chen, L. Mao, *Angew. Chem. Int. Ed.* **2023**, *62*, e202216720; d) B. Su, J. Jin, K. Han, Z. Xia, *Adv. Funct. Mater.* **2023**, *33*, 2210735.
- [7] a) Q. He, C. Zhou, L. Xu, S. Lee, X. Lin, J. Neu, M. Worku, M. Chaaban, B. Ma, *ACS Materials Lett.* **2020**, *2*, 633–638; b) Z. Li, Y. Li, P. Liang, T. Zhou, L. Wang, R.-J. Xie, *Chem. Mater.* **2019**, *31*, 9363–9371; c) C. Zhou, H. Lin, Y. Tian, Z. Yuan, R. Clark, B. Chen, L. J. van de Burgt, J. C. Wang, Y. Zhou, K. Hanson, *Chem. Sci.* **2018**, *9*, 586–593; d) C. Zhou, M. Worku, J. Neu, H. Lin, Y. Tian, S. Lee, Y. Zhou, D. Han, S. Chen, A. Hao, *Chem. Mater.* **2018**, *30*, 2374–2378; e) Z.-P. Wang, J.-Y. Wang, J.-R. Li, M.-L. Feng, G.-D. Zou, X.-Y.

- Huang, *Chem. Commun.* **2015**, *51*, 3094–3097; f) Z. Wang, D. Xie, F. Zhang, J. Yu, X. Chen, C. P. Wong, *Sci. Adv.* **2020**, *6*, eabc2181.
- [8] a) B. Su, S. Geng, Z. Xiao, Z. Xia, *Angew. Chem. Int. Ed.* **2022**, *61*, e202208881; b) B. Su, M. Li, E. Song, Z. Xia, *Adv. Funct. Mater.* **2021**, *31*, 2105316.
- [9] a) K. M. McCall, V. Morad, B. M. Benin, M. V. Kovalenko, *ACS Materials Lett.* **2020**, *2*, 1218–1232; b) J.-H. Wei, J.-F. Liao, L. Zhou, J.-B. Luo, X.-D. Wang, D.-B. Kuang, *Sci. Adv.* **2021**, *7*, eabg3989.
- [10] V. Morad, S. Yakunin, M. V. Kovalenko, *ACS Materials Lett.* **2020**, *2*, 845–852.
- [11] M. Li, Z. Xia, *Chem. Soc. Rev.* **2021**, *50*, 2626–2662.
- [12] H. Peng, X. He, Q. Wei, Y. Tian, W. Lin, S. Yao, B. Zou, *ACS Appl. Mater. Interfaces* **2022**, *14*, 45611–45620.
- [13] J. L. Li, Y. F. Sang, L. J. Xu, H. Y. Lu, J. Y. Wang, Z. N. Chen, *Angew. Chem. Int. Ed.* **2022**, *134*, e202113450.
- [14] Q. Wei, T. Chang, R. Zeng, S. Cao, J. Zhao, X. Han, L. Wang, B. Zou, *J. Phys. Chem. Lett.* **2021**, *12*, 7091–7099.
- [15] a) X. Cheng, Z. Xie, W. Zheng, R. Li, Z. Deng, D. Tu, X. Shang, J. Xu, Z. Gong, X. Li, *Adv. Sci.* **2022**, *9*, 2103724; b) R. Zhang, X. Xu, X. Mao, Z. Wang, P. Wang, Y. Yang, J. Chen, R. Lu, W. Deng, K. Han, *Laser Photonics Rev.* **2022**, *16*, 2100689.
- [16] a) H. L. Xuan, J. L. Li, L. J. Xu, D. S. Zheng, Z. N. Chen, *Adv. Opt. Mater.* **2022**, *10*, 2200591; b) J. Yin, R. Naphade, L. G. Arzaluz, J.-L. Brédas, O. M. Bakr, O. F. Mohammed, *ACS Energy Lett.* **2020**, *5*, 2149–2155; c) T. Schmidt, K. Lischka, W. Zulehner, *Phys. Rev. B: Condens. Matter Mater. Phys.* **1992**, *45*, 8989–8994; d) Q. Zhang, Y. Ji, Z. Chen, D. Vella, X. Wang, Q.-H. Xu, Y. Li, G. Eda, *J. Phys. Chem. Lett.* **2019**, *10*, 2869–2873.
- [17] D.-Y. Li, J.-H. Song, Z.-Y. Xu, Y.-J. Gao, X. Yin, Y.-H. Hou, L.-J. Feng, C.-Y. Yue, H. Fei, X.-W. Lei, *Chem. Mater.* **2022**, *34*, 6985–6995.
- [18] a) Z. Ma, X. Ji, S. Lin, X. Chen, D. Wu, X. Li, Y. Zhang, C. Shan, Z. Shi, X. Fang, *Adv. Mater.* **2023**, 2300731; b) Y. Hui, S. Chen, R. Lin, W. Zheng, F. Huang, *Mater. Chem. Front.* **2021**, *5*, 7088–7107.
- [19] Y. Jing, Y. Liu, M. Li, Z. Xia, *Adv. Opt. Mater.* **2021**, *9*, 2002213.
- [20] Z. Qi, Y. J. Ma, D. Yan, *Aggregate* **2023**, e411.
- [21] a) B. Zhou, Z. Qi, M. Dai, C. Xing, D. Yan, *Angew. Chem. Int. Ed.* **2023**, e202309913; b) F. Liu, T. Zhang, D. Mondal, S. Teng, Y. Zhang, K. Huang, D. Wang, W. Yang, P. Mahadevan, Y. S. Zhao, *Angew. Chem. Int. Ed.* **2021**, *133*, 13660–13665; c) Y. Deng, X. Liang, F. Li, M. Wang, Z. Zhou, J. Zhao, F. Wang, S. Liu, Q. Zhao, *Laser Photonics Rev.* **2023**, 2300043.
- [22] a) K.-J. Li, Y.-Y. Zhao, M.-E. Sun, G.-S. Chen, C. Zhang, H.-L. Liu, H.-Y. Li, S.-Q. Zang, T. C. Mak, *Cryst. Growth Des.* **2022**, *22*, 3295–3302; b) L. Lian, T. Zhang, H. Ding, P. Zhang, X. Zhang, Y.-B. Zhao, J. Gao, D. Zhang, Y. S. Zhao, J. Zhang, *ACS Materials Lett.* **2022**, *4*, 1446–1452; c) B. Zhou, G. Xiao, D. Yan, *Adv. Mater.* **2021**, *33*, 2007571; d) X. Yang, L. Ma, D. Yan, *Chem. Sci.* **2019**, *10*, 4567–4572.
- [23] Deposition Numbers 2347582, 2347511 and 2347509 contain the supplementary crystallographic data for compounds 1, 2, and 3, respectively. These data are provided free of charge by the joint Cambridge Crystallographic Data Centre and Fachinformationszentrum Karlsruhe Access Structures service.

Manuscript received: February 28, 2024

Accepted manuscript online: April 14, 2024

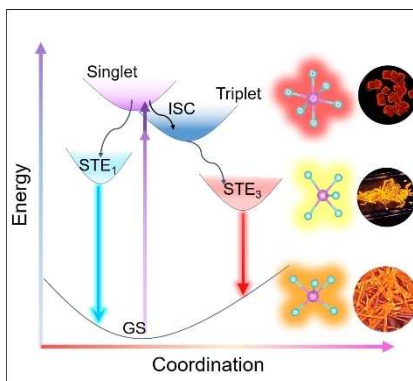
Version of record online: ■■■, ■■■

Forschungsartikel

Emissive Metal Halides

J.-F. Liao, Z. Zhang, L. Zhou, Z. Tang,
G. Xing* [e202404100](#)

Achieving Near-Unity Red Light Photoluminescence in Antimony Halide Crystals via Polyhedron Regulation



Three $(\text{TMS})_2\text{SbCl}_3$ crystals have been prepared with diverse $[\text{SbCl}_3]^{2-}$ configurations and distinct emission color (i.e., red, orange, and yellow) through solvent engineering. It is found that higher coordination symmetry and longer Sb...Sb distance are in favor of the larger Stokes shift and lower energy emission. This work sheds insights into the structure-photoluminescence relationship towards development of highly efficient optoelectronic materials.